

# Toward Controlling Filament Size and Location for Resistive Switches via Nanoparticle Exsolution at Oxide Interfaces

Jonathan Spring, Eva Sediva, Zachary D. Hood, Juan Carlos Gonzalez-Rosillo, Willis O'Leary, Kun Joong Kim, Alfonso J. Carrillo, and Jennifer L. M. Rupp\*

Memristive devices are among the most prominent candidates for future computer memory storage and neuromorphic computing. Though promising, the major hurdle for their industrial fabrication is their device-to-device and cycle-to-cycle variability. These occur due to the random nature of nanoionic conductive filaments, whose rupture and formation govern device operation. Changes in filament location, shape, and chemical composition cause cycle-to-cycle variability. This challenge is tackled by spatially confining conductive filaments with Ni nanoparticles. Ni nanoparticles are integrated on the bottom  $\text{La}_{0.2}\text{Sr}_{0.7}\text{Ti}_{0.9}\text{Ni}_{0.1}\text{O}_{3-\delta}$  electrode by an exsolution method, in which, at high temperatures under reducing conditions, Ni cations migrate to the perovskite surface, generating metallic nanoparticles. This fabrication method offers fine control over particle size and density and ensures strong particle anchorage in the bottom electrode, preventing movement and agglomeration. In devices based on amorphous  $\text{SrTiO}_3$ , it is demonstrated that as the exsolved Ni nanoparticle diameter increases up to  $\approx 50$  nm, the ratio between the ON and OFF resistance states increases from single units to 180 and the variability of the low resistance state reaches values below 5%. Exsolution is applied for the first time to engineer solid–solid interfaces extending its realm of application to electronic devices.

## 1. Introduction

Nanoionic memristive devices are counted among the most promising technologies to replace current transistor-based computer architectures. They offer sub-nanosecond switching speeds,<sup>[1]</sup> scaling potential down to  $4\text{ nm}^2$ ,<sup>[2]</sup> and in-memory computation capabilities due to their nonvolatility.<sup>[3]</sup> Their applications range from binary memory storage<sup>[4]</sup> to neuromorphic computing hardware for implementing learning algorithms based on neural networks.<sup>[5–7]</sup> Though promising, the major hurdle for their industrial fabrication is device-to-device and cycle-to-cycle variability. In metal–oxide-based memristive devices, a switching oxide is sandwiched between two metal electrodes and changes its resistance with an application of a voltage in a bipolar manner. Most switching mechanisms rely on locally reducing the switching oxide thereby forming a filamentary region rich in oxygen vacancies. Different resistance states can be accessed by formation and

rupture of these conductive filaments. In a conventional planar metal–oxide–metal device, conductive filaments are seeded stochastically and homogeneously over the whole device area. Uncontrolled, this process results in unpredictable filament location, shape, size, and composition. During operation, local changes in the filament stoichiometry and changes of the active filament location give rise to the observed cycle-to-cycle variability.<sup>[8]</sup> For uniform and reproducible switching, it is therefore necessary to control the filament both during the seeding and operation processes.

In order to address the challenge of stochastic filament location, several strategies have been put forward to spatially confine filaments either in the switching or electrode materials. These include 1) switching within a single dislocation in  $\text{SrTiO}_3$ <sup>[9]</sup> and in  $\text{SiGe}$ ,<sup>[10]</sup> 2) fabricating electrodes into tips,<sup>[11–18]</sup> 3) integrating nanoporous graphene into the switching material,<sup>[19–22]</sup> 4) embedding nanoparticles into the switching material,<sup>[23–33]</sup> 5) introducing nanoparticles at the metal–oxide interface,<sup>[34–40]</sup> and 6) engineering the edges of the devices, which has been shown to be industrially viable.<sup>[41]</sup> These strategies are analyzed in terms of their opportunities, processing challenges and materials universality in **Table 1**, and summarized through device

J. Spring, Dr. E. Sediva, Dr. Z. D. Hood, Dr. J. C. Gonzalez-Rosillo, W. O'Leary, Dr. K. J. Kim, Dr. A. J. Carrillo, Prof. J. L. M. Rupp  
Electrochemical Materials  
Department of Materials Science and Engineering  
Massachusetts Institute of Technology  
77 Massachusetts Av., Cambridge, MA 02139, USA  
E-mail: jrupp@mit.edu

J. Spring, Dr. E. Sediva, Prof. J. L. M. Rupp  
Electrochemical Materials  
Department of Materials  
ETHZ  
Hönggerbergring 64, Zurich 8093, Switzerland

Prof. J. L. M. Rupp  
Electrochemical Materials  
Department of Electrical Engineering and Computer Science  
Massachusetts Institute of Technology  
77 Massachusetts Av., Cambridge, MA 02139, USA

 The ORCID identification number(s) for the author(s) of this article can be found under <https://doi.org/10.1002/sml.202003224>.

DOI: 10.1002/sml.202003224

**Table 1.** Overview of various fabrication techniques and methods for filament confinement in memristive devices.

| Confinement strategy                         | Location of confining structure                | Switching oxide material       | Dimension and material of confinement structures | Processing method of confinement structures                         | Universality of method  | Processing complexity  |   | Ref.      |
|--|--|--------------------------------|--|---|---|--|---|-----------|
|  |  |                                |  |   |   | Advantage  | Disadvantage  |           |
| Nanoparticles embedded in the switching film |  |                                |  |   |   |  |   |           |
|  | Switching oxide                                | HfO <sub>2</sub>               | ∅ = 30–90 nm (Ag, Ti, Pt)                        | Template-directed fabrication                                       | Yes   | Control over particle size and position and easy upscaling                           | Three deposition steps needed   | [23]      |
|  | Switching oxide                                | ZrO <sub>2</sub>               | ∅ ≈ 10 nm (Au)                                   | Electron beam evaporation of Au, postannealing at 700–900 °C        | Not applicable to amorphous switching oxides                      | Universality of particle material  | High-temperature postannealing crystallizes the switching film                                  | [31]      |
|  | Switching oxide                                | TiO <sub>2</sub>               | ∅ ≈ 5 nm (Pt)                                    | Sputtering of Pt, postannealing at 500 °C                           | Not applicable to amorphous switching oxides                      | Universality of particle material  | High-temperature postannealing crystallizes the switching film                                  | [25]      |
|  | Switching oxide                                | TiO <sub>2</sub>               | ∅ ≈ 15 nm (Ru)                                   | Atomic layer deposition of Ru                                       | Not clear, two phases of switching oxide required                 | Switching could be independent of particle material                                  | Device performance depends on TiO <sub>2</sub> crystal structure                                | [30]      |
|  | Switching oxide                                | Al <sub>2</sub> O <sub>3</sub> | ∅ ≈ 1.3 nm (IrO <sub>x</sub> )                   | Sputtering of IrO <sub>x</sub>                                      | Not clear, core-shell oxide particles needed                      | IrO <sub>x</sub> form an oxygen rich shell layer aiding the switching mechanism      | Universality of particle material is not clear  | [24]      |
|  | Switching oxide and their electrode interfaces | TiO <sub>2</sub>               | ∅ ≈ 1.3 nm (Pt)                                  | Sputtering of Pt  | Yes, for sputtering compatible materials                          | Particles and switching oxide grown with a single method without breaking vacuum     | Low control over particle distribution  | [32]      |
| Nanoparticles at the electrode interface     |  |                                |  |   |   |  |   |           |
|  | Electrode-switching oxide interface            | SrTiO <sub>3</sub>             | ∅ ≈ 10–50 nm (Ni)                                | Metal particle exsolution   | Applicable with exsolvable bottom electrodes                      | Particle anchorage, spontaneous bottom-up fabrication                                | Limited to electrodes with exsolution capabilities  | This work |
|  | Bottom electrode                               | SrTiO <sub>3</sub>             | ∅ ≈ 15 nm (Au)                                   | Electrostatic immobilization of citrate-stabilized Au nanoparticles | Yes   | Universality of materials for nanoparticles and switching oxide                      | Separate synthesis for Au particles is needed and they are not anchored to the bottom electrode | [36]      |
|  | Bottom electrode                               | ZrO <sub>2</sub>               | ∅ ≈ 20–50 nm (Cu)                                | Electron beam evaporation of Cu and postannealing at 600 °C         | Not applicable to amorphous switching oxides                      | Universality of particle material  | Need of high-temperature processing of the switching material                                   | [34]      |
|  | Bottom electrode                               | ZnO                            | ∅ ≈ 20 nm (Ag)                                   | Pulsed laser deposition (PLD)                                       | Yes, for PLD-compatible materials                                 | Particles and switching oxide grown with a single method without breaking vacuum     | Particles are not anchored to the bottom electrode  | [37]      |
|  | Bottom electrode                               | NiO                            | ∅ ≈ 15 nm (Au)                                   | Bio-nanofabrication   | No, requires porter proteins, which bind to the particle material | Precise positioning of nanoparticles   | Nonuniform oxide growth (high density of grain boundaries) on top of the particles              | [38]      |
|  | Top electrode                                  | ZnO                            | ∅ ≈ 4 nm (Ag)                                    | Ag sputtering   | Not clear, requires electromigration of particle material ions    | No additional deposition steps (particle layer is cosputtered with bottom electrode) | Migration of particles to top electrode requires several switching cycles                       | [39]      |
|  | Bottom electrode                               | Al <sub>2</sub> O <sub>3</sub> | ∅ ≈ 14 nm (Ag)                                   | Spin coating  | Yes   | Uniform size of nanoparticles  | Separate synthesis step is needed to fabricate Ag particles                                     | [35]      |

**Table 1.** Continued.

| Confinement strategy   | Location of confining structure     | Switching oxide material       | Dimension and material of confinement structures                | Processing method of confinement structures               | Universality of method  | Processing complexity                            |   | Ref. |
|------------------------|-------------------------------------|--------------------------------|---|---|---|--|---|------|
|                        |                                     |                                |   |   |   | Advantage  | Disadvantage  |      |
| Nanoporous graphene    |                                     |                                |   |   |   |  |   |      |
|                        | Electrode–switching oxide interface | Ta <sub>2</sub> O <sub>5</sub> | Pore $\varnothing \approx 25\text{--}100$ nm                    | Electron beam lithography                                 | Yes   | Precise control of filament size and position    | Difficult to scale up electron beam lithography                               | [19] |
|                        | Electrode–switching oxide interface | HfO <sub>x</sub>               | Pore $\varnothing \approx 45$ nm                                | Electron beam lithography                                 | Yes   | Precise control of filament size and position    | Difficult to scale up electron beam lithography                               | [22] |
| Single dislocation     |                                     |                                |   |   |   |  |   |      |
|                        | Switching oxide                     | SrTiO <sub>3</sub>             | 1–2 nm  | Single dislocations                                       | Only for single crystalline switching oxides                                  | Extremely high device density                    | Difficult to scale up   | [9]  |
|                        | Switching oxide                     | SiGe                           | 5–10 nm   | Dislocation generation by defect-selective etching        | Yes   | Extremely high device density                    | Difficult to scale up   | [10] |
| Electrode shaping      |                                     |                                |   |   |   |  |   |      |
|                        | Switching oxide                     | SiO <sub>2</sub>               | Tip $\varnothing < 10$ nm (Ag)                                  | Solvent-assisted nanotransfer printing                    | Difficult to apply beyond SiO <sub>2</sub>                                    | Strong electric field concentration              | Requires precise etching of switching oxide                                   | [15] |
|                        | Electrode                           | Al <sub>2</sub> O <sub>3</sub> | Tip $\varnothing = 50$ nm (Ag)                                  | Template stripping  | Difficult to apply beyond SiO <sub>2</sub>                                    | Low-cost high-throughput process                 | Limited to low temperature switching oxide processing                         | [13] |
|                        | Electrode                           | Al <sub>2</sub> O <sub>3</sub> | Tip $\varnothing \approx 40$ nm (Cu)                            | Template stripping  | Difficult to apply beyond SiO <sub>2</sub>                                    | Low-cost high-throughput process                 | Device design is not flexible   | [14] |
|                        | Electrode                           | HfO <sub>2</sub>               | Tip $\varnothing \approx 120$ nm (CoSi <sub>2</sub> )           | Standard microfabrication                                 | Yes   | Compatible with standard industrial processes    | Fabrication includes many steps   | [11] |
|                        | Electrode                           | TiO <sub>2</sub>               | Tip $\varnothing \approx 100$ nm (Cu)                           | Wet-etching using a dot-shape photoresist mask            | Limited to electrochemical metallization cells and low temperature processing | Cation injection control and field concentration | Limited to electrochemical metallization cells and low temperature processing | [18] |
|                        | Electrode and switching oxide       | Ta <sub>2</sub> O <sub>5</sub> | Column interspacing <5 nm (Fe <sub>3</sub> O <sub>4</sub> , Ta) | Process parameter variation during PLD                    | Yes, for PLD-compatible materials   | Simple fabrication process                       | Requirements on materials compatibility                                       | [17] |
|                        | Substrate                           | HfO <sub>2</sub>               | Tip $\varnothing = 50$ nm                                       | Ion irradiation and replica molding process               | Only for flexible substrates  | Low-cost high-throughput process                 | Requires flexible substrate   | [16] |
| Engineering cell edges |                                     |                                |   |   |   |  |   |      |
|                        | Edges of switching bit/cell         | TaO <sub>x</sub>               | Invalidation and protection of cell edges, 40 nm cell size      | Low damage etching, side cell oxidation and encapsulation | Yes   | Industrially viable                              | Advanced fabrication methods required   | [41] |

The table focuses on oxide switching materials, memory applications and the methods outlined in Figure 1a. The authors are aware that other confinement methods and reports exist. This table provides an overview of different fabrication routes rather than an exhaustive literature survey.

sketches in **Figure 1a**. To date, integration of nanoparticles is one of the most popular techniques to seed and localize the filament, and thereby improve the variability of the switching parameters. The localizing effect is usually thought to be due to a local field enhancement near the nanoparticles, which can

trigger material reduction by attracting oxygen vacancies.<sup>[35]</sup> In the following section, we highlight the critical aspects of nanoparticle integration including the deposition technique, material, and size/density control, all of which are reviewed in Table 1.

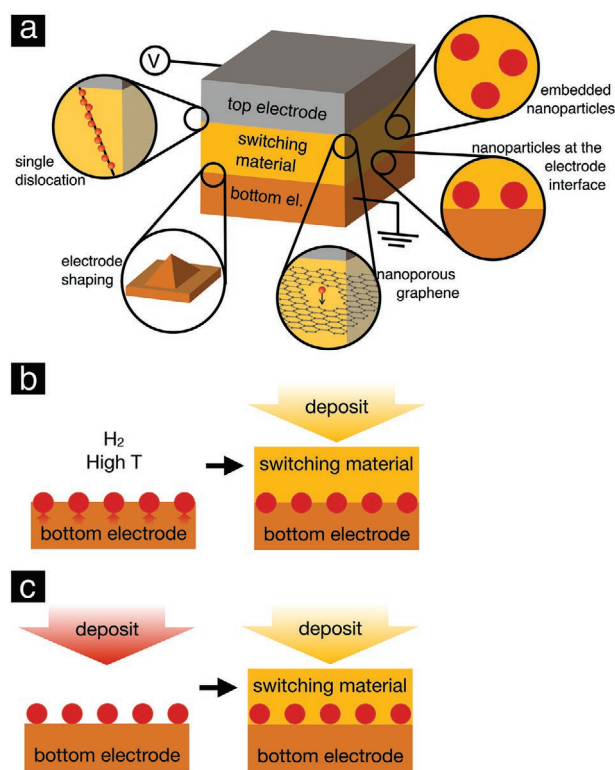


**Figure 1.** a) Schematic summarizing strategies to confine conductive filaments in memristive devices. These include particles embedded in the switching material, particles at the electrode–switching material interface, channels for conductive ions in graphene, pyramidal electrodes and single dislocations defining paths for ion migration. b,c) Schematics showing processes for introducing nanoparticles at the electrode–switching oxide interface. With exsolution the particle formation is intrinsic to the process b), whereas traditionally an extra deposition step is needed c).

### 1.1. Nanoparticles at the Bottom Electrode–Switching Material Interface to Confine Conductive Filaments

Nanoparticles at the electrode interface are often integrated into the device by depositing ultrathin metallic films—via electron beam evaporation,<sup>[34]</sup> pulsed laser deposition,<sup>[37]</sup> or sputtering<sup>[32]</sup> and utilizing island growth. Another option is to disperse previously synthesized nanoparticles by spin coating<sup>[35]</sup> or electrostatic immobilization by organic aids.<sup>[36]</sup> All of these deposition methods, however, leave the particles loose, making particle floating a possibility, and can distort the switching film.<sup>[36]</sup> Elaborate anchoring methods have been proposed to fix the nanoparticles to the bottom electrode. For example Au nanoparticles were delivered to a Ti-patterned bottom electrode by a porter protein with a Ti binding peptide.<sup>[38]</sup>

In terms of the nanoparticle material, Ag<sup>[35,37,39,40]</sup> or Au<sup>[36,38]</sup> have proved to be most popular, though the use of Pt,<sup>[23,42]</sup> Ru,<sup>[29]</sup> Cu,<sup>[34]</sup> or Co<sup>[43]</sup> has been reported as well. In the case of Ag or Cu nanoparticles, metal ions often migrate into the oxide during operation, actively taking part in the switching mechanism.<sup>[7,26,39,44]</sup> For noble metals, it is often assumed that the nanoparticles serve predominantly to enhance the local electric field. Just like movement of metal cations can participate in

switching, oxygen anion exchange with the electrodes can benefit the stability of the switching process.<sup>[45]</sup> Considering this point, it would be beneficial to integrate nanoparticles acting as an ohmic electrode with the ability to exchange oxygen during the device operation, as demonstrated for example with Ti nanoparticles in HfO<sub>x</sub> ( $x < 2$ ).<sup>[23]</sup> In this case, two mechanisms can stabilize the switching process simultaneously. The nanoparticles both localize the filament spatially and keep the local oxygen stoichiometry stable by enabling oxygen exchange with the nanoparticle during device operation. Here, we propose the integration of Ni nanoparticles in combination with SrTiO<sub>3</sub> switching oxide to take advantage of this stabilization process.

The effect of the nanoparticle size and density on the switching properties both illuminates how the nanoparticle is involved in device operation and provides an engineering strategy to optimize device performance. Different nanoparticle sizes have been investigated, for example with ZnO and Al<sub>2</sub>O<sub>3</sub> as switching oxides. In ZnO particle diameters of 20 nm resulted in stable switching, whereas 40 and 80 nm diameter particles resulted in substantial leakage currents.<sup>[37]</sup> In Al<sub>2</sub>O<sub>3</sub>, stable switching was observed only with particle diameters between 5 and 20 nm with an optimum at 14 nm.<sup>[35]</sup> Still, the effect of the size of the nanoparticle on the switching properties remains unclear. The nanoparticle density was investigated using SrTiO<sub>3</sub> as the switching oxide and Au nanoparticles. Higher density changed the growth model of SrTiO<sub>3</sub> from layer-by-layer to island growth, increasing the film roughness.<sup>[36]</sup> However, the effects on the switching properties remain unknown.

### 1.2. Exsolution as a Novel Processing Technique for Nanoparticle Integration into Switching Oxides

A promising, yet untested route to introduce nanoparticles at the electrode–switching oxide interface is metal cation exsolution from a bottom oxide electrode. In general, exsolution<sup>[46]</sup> refers to the process of forming catalytically active metal nanoparticles anchored into the surface of metal oxides. The exsolution process has found many applications, including automotive exhaust control,<sup>[47]</sup> sensors,<sup>[48]</sup> thermocatalytic processes,<sup>[49]</sup> and solid oxide fuel/electrolysis cells,<sup>[50]</sup> all of which are examples for functionalizing a surface in order to improve gas–solid kinetics. Exsolution of a metal oxide is carried out via thermal treatment under a reducing atmosphere (e.g., H<sub>2</sub>). Under reducing conditions, metal cations in certain metal oxides—commonly B-site cations in perovskite oxides ABO<sub>3</sub>—segregate to the oxide surface, undergo reduction, and nucleate into metallic nanoparticles.<sup>[51,52]</sup> Exsolution processing is unique in that it produces nanoparticles partially immersed in the oxide host, as diagrammed in Figure 1b. This process is in stark contrast to particles deposited through conventional means, which sit atop the oxide host (Figure 1c). Exsolution is favored by high reducibility of the metal cation; Pd<sup>4+</sup>, Pt<sup>4+</sup>, Rh<sup>4+</sup>,<sup>[53]</sup> Ni<sup>2+</sup>, and Fe<sup>3+</sup><sup>[50]</sup> cations have been commonly exsolved from oxide perovskites. In catalysis applications, partial immersion of the nanoparticles affords resistance to agglomeration and catalyst poisoning, both of which impact performance.<sup>[54]</sup> More relevant to the nanoparticle-switching oxide pairs is the ability to tune

exsolved particle size, density, anchorage, and composition<sup>[54]</sup> to stabilize and improve switching performance. However, exsolution has been so far utilized mainly in catalysis on gas–solid interfaces. In this study we aim to use exsolution to promote ion exchange at solid–solid interfaces, substantially extending the possible realms of application of exsolution.

In this work we explore for the first time the effect of exsolving metal nanoparticles at the electrode–switching oxide interface on the memristive switching response in devices based on amorphous SrTiO<sub>3</sub>. The main advantages of fabricating metal nanoparticles by the exsolution method are their anchoring in the electrode backbone, the lack of additional deposition and synthesis steps and the control over their size and density by the duration and temperature of the exsolution process. Despite these advantages, exsolution has so far not been used in electronic devices or to engineer solid–solid interfaces. We focus on the feasibility of device fabrication and the effect on the switching properties, specifically the cycle-to-cycle variability. For this application, we fabricated memristive devices based on a La<sub>0.2</sub>Sr<sub>0.7</sub>Ti<sub>0.9</sub>Ni<sub>0.1</sub>O<sub>3-δ</sub> bottom electrode, which can efficiently exsolve Ni particles at the interface with the amorphous SrTiO<sub>3</sub> (switching oxide). We investigated the effect of the exsolved Ni particle size and density by adjusting time and temperature to control the exsolution level and nanostructure at the bottom electrode interface.

With the integration of exsolved Ni nanoparticles, we demonstrate a new level of control over the cycle-to-cycle variability of the devices by confining and controlling the local conductive filaments spatially, and also controlling the filament rupture and formation. Memristive devices with exsolved nanoparticles can have major technological relevance, as the variability, currently one of the biggest hurdles for the industrial implementation of memristive device technology, can be effectively tuned.

## 2. Results and Discussion

### 2.1. Exsolved Memristive Device Structure Concept

The core of our memristive device design are Ni nanoparticles, which confine the filament in the SrTiO<sub>3</sub> switching oxide. In order to integrate the Ni nanoparticles into the switching oxide, we exsolve them from the La<sub>0.2</sub>Sr<sub>0.7</sub>Ti<sub>0.9</sub>Ni<sub>0.1</sub>O<sub>3-δ</sub> bottom electrode surface before capping with a SrTiO<sub>3</sub> switching oxide. The bottom electrode was deposited on a lattice matched LaAlO<sub>3</sub> substrate, which ensured a smooth electrode–switching oxide interface.<sup>[52]</sup> A smooth interface was essential so that a) the nanoparticles were the sole surface aberrations and b) the SrTiO<sub>3</sub> switching oxide could homogeneously cover the particles. Last, we capped the exsolved La<sub>0.2</sub>Sr<sub>0.7</sub>Ti<sub>0.9</sub>Ni<sub>0.1</sub>O<sub>3-δ</sub>–SrTiO<sub>3</sub> film stack with sputtered Pt electrodes (Figure 2a).

We first investigated the microstructure of the individual device layers by transmission electron microscopy (TEM). The device cross section, as shown in Figure 2b, confirmed the growth of dense SrTiO<sub>3</sub> and La<sub>0.2</sub>Sr<sub>0.7</sub>Ti<sub>0.9</sub>Ni<sub>0.1</sub>O<sub>3-δ</sub> films separated by a continuous interface with a low roughness of about 2–4 nm. The fast Fourier transform (FFT) of the SrTiO<sub>3</sub> layer demonstrated, that the switching oxide had no crystalline order,

while the FFT of the La<sub>0.2</sub>Sr<sub>0.7</sub>Ti<sub>0.9</sub>Ni<sub>0.1</sub>O<sub>3-δ</sub> bottom electrode had features corresponding to the (110), (200), and (220) crystalline planes typical for a crystalline perovskite structure. The TEM results provided the first confirmation, that the deposited La<sub>0.2</sub>Sr<sub>0.7</sub>Ti<sub>0.9</sub>Ni<sub>0.1</sub>O<sub>3-δ</sub> was highly crystalline whereas the deposited SrTiO<sub>3</sub> switching oxide was amorphous.

To further access the crystallinity of the thin films, we performed X-ray diffraction (XRD) on the individual layers (exsolved La<sub>0.2</sub>Sr<sub>0.7</sub>Ti<sub>0.9</sub>Ni<sub>0.1</sub>O<sub>3-δ</sub> and SrTiO<sub>3</sub>), both deposited on LaAlO<sub>3</sub>. In the La<sub>0.2</sub>Sr<sub>0.7</sub>Ti<sub>0.9</sub>Ni<sub>0.1</sub>O<sub>3-δ</sub> pattern (Figure 2c), the peaks at  $2\theta = 45.8^\circ$  and  $47.95^\circ$  corresponded to the (200) reflections of the film and substrate respectively. The absence of any other film reflections confirmed the highly oriented growth of the electrode. Meanwhile, the XRD pattern of the SrTiO<sub>3</sub> film deposited on LaAlO<sub>3</sub>, as shown in Figure 2c, possessed only one strong (200) reflection attributed to the substrate with no other features. This outcome was thanks to the low deposition temperature (150 °C), which resulted in an amorphous film. All in all, the XRD analyses was in agreement with the TEM analyses.

The smoothness of the La<sub>0.2</sub>Sr<sub>0.7</sub>Ti<sub>0.9</sub>Ni<sub>0.1</sub>O<sub>3-δ</sub> electrode was further confirmed by atomic force microscopy (AFM) (Figure S1, Supporting Information). A low root-mean-square surface roughness of 1.5 nm was measured.

We performed exsolution on La<sub>0.2</sub>Sr<sub>0.7</sub>Ti<sub>0.9</sub>Ni<sub>0.1</sub>O<sub>3-δ</sub> by films by annealing them at 900 °C for 10 h in a 5% H<sub>2</sub>/Ar atmosphere. We then investigated the resulting particles with scanning electron microscopy (SEM). A top down micrograph of the exsolved La<sub>0.2</sub>Sr<sub>0.7</sub>Ti<sub>0.9</sub>Ni<sub>0.1</sub>O<sub>3-δ</sub> layer (Figure 2d) confirmed the homogeneous distribution of spherical nanoparticles over the entire surface of the thin film. Further image analysis revealed an average nanoparticle diameter of  $31 \pm 6$  nm. We next interrogated the exsolved particles via scanning transmission electron microscopy (STEM) coupled with energy dispersive X-ray spectroscopy (EDS) on a sample of an exsolved La<sub>0.2</sub>Sr<sub>0.7</sub>Ti<sub>0.9</sub>Ni<sub>0.1</sub>O<sub>3-δ</sub> thin film prepared via focused ion beam (FIB) lift out. Figure 2e shows a high-angle annular dark-field STEM image of an exsolved Ni particle embedded in this sample. EDS elemental mapping of this sample revealed an exsolved particle mainly composed of Ni embedded in a perovskite mainly composed of La, Sr, Ti, and also Ni (as expected). Next, we performed an EDS line scan to quantify the relative distributions of La, Sr, Ti, and Ni within the perovskite backbone and the exsolved Ni particle (Figure S2, Supporting Information). Within the perovskite backbone, the concentrations of Sr and Ti were higher than the concentrations of La and Ni, as expected given the stoichiometry of the perovskite. It was clear that the exsolved Ni particle was embedded in the perovskite backbone, indicating that the exsolved nanoparticles were intimately anchored to the surface of the perovskite.

After the successful decoration of La<sub>0.2</sub>Sr<sub>0.7</sub>Ti<sub>0.9</sub>Ni<sub>0.1</sub>O<sub>3-δ</sub> with Ni nanoparticles via exsolution, we measured the film resistivity to ensure its utility as a bottom electrode material. The sheet resistance after exsolution was determined by a four-probe measurement using the Van der Pauw method with Pt contacts to be  $36 \Omega \square^{-1}$ , well within the useful range.

With the materials characterized and the successful fabrication of exsolved La<sub>0.2</sub>Sr<sub>0.7</sub>Ti<sub>0.9</sub>Ni<sub>0.1</sub>O<sub>3-δ</sub>/Ni/SrTiO<sub>3</sub>/Pt devices, we characterize the switching properties of the devices by cyclic voltammetry.

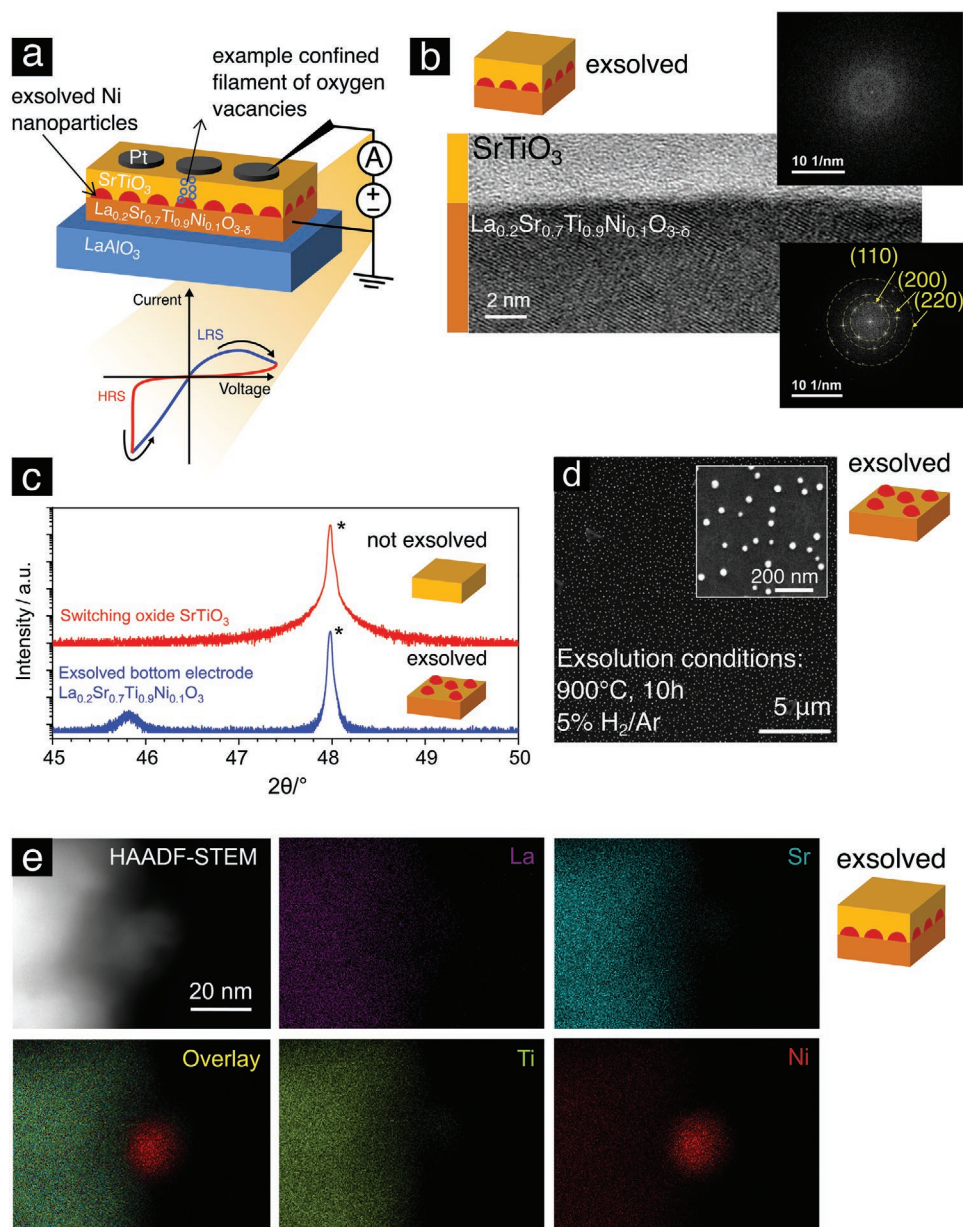


**Figure 2.** a) Current device design with a schematic of its current–voltage response. b) Cross-section TEM micrograph of a device incorporating exsolved Ni nanoparticles. c) X-ray diffraction pattern of  $\text{La}_{0.2}\text{Sr}_{0.7}\text{Ti}_{0.9}\text{Ni}_{0.1}\text{O}_{3-\delta}$  and amorphous  $\text{SrTiO}_3$  thin films on  $\text{LaAlO}_3$ . The spectra are recorded around the  $\text{LaAlO}_3$  (200) substrate peak (\*). d) Top-view SEM micrograph of a  $\text{La}_{0.2}\text{Sr}_{0.7}\text{Ti}_{0.9}\text{Ni}_{0.1}\text{O}_{3-\delta}$  thin film after reduction for 10 h at 900 °C. The exsolved Ni nanoparticles are clearly visible as bright spots on the dark perovskite backbone. e) High-angle annular dark-field scanning transmission electron microscopy (HAADF-STEM) image of the anchored nanoparticle and EDS elemental mapping of the particle and bottom electrode.

## 2.2. An Exsolved Memristive Device to Control Cycle-to-Cycle Variability

To characterize the electrical response and performance of the device, we performed quasistatic cyclic voltammetry. Before cycling, the devices were electroformed at a limiting current of 1 mA for 30 s. The resulting current over time plots are shown in Figure S3 (Supporting Information). The current–voltage ( $I$ – $V$ ) response from cyclic voltammetry, presented in Figure 3a, exhibited a hysteresis of counter-eightwise polarity with a sharp set and a gradual reset transition. This behavior is characteristic

of a switching mechanism based on the internal rupture and formation of conductive filaments.<sup>[55,56]</sup> Importantly, the  $I$ – $V$  curves showed very little cycle-to-cycle deviations over 1000 cycles, an exciting result also evident from the evolution of the high and low resistance states during cycling (Figure 3b). The device-to-device variation is shown in Figure S4 (Supporting Information). Given these  $I$ – $V$  curves, we were encouraged by the highly stable operation of our exsolved memristive device.

In order to investigate how the Ni nanoparticles contributed to the device's switching performance and stability, we varied the particle size and density and measured the changes on

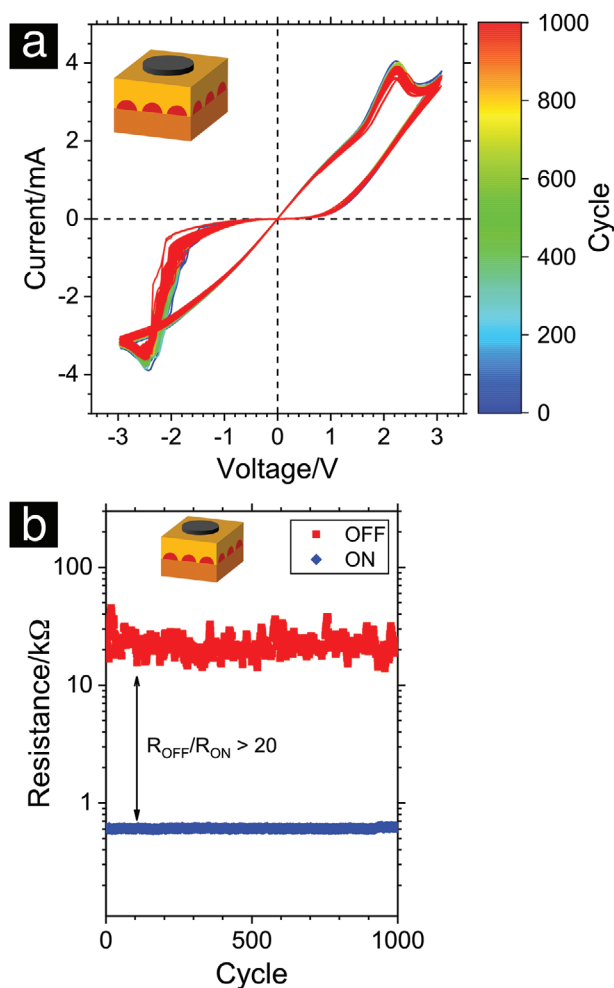


**Figure 3.** a) Current–voltage response for 1000 consecutive switching cycles. The device included exsolved Ni nanoparticles with an average diameter of 31 nm. b) Evolution of the resistance values for the OFF and ON states for the switching cycles shown in (a).

switching properties. To change particle properties, we tailored the exsolution time and temperature. A combination of three different exsolution temperatures (800, 900, and 1000 °C) and two different times (5 and 10 h) was chosen to cover a wide range of Ni particle sizes and densities. XRD patterns were collected for each time and temperature combination (Figure S5, Supporting Information). The SEM images in **Figure 4a** exemplify the influence of the reduction conditions on nanoparticles size and density. The dark regions are the perovskite backbone and the bright spots are the exsolved nanoparticles. From SEM analysis we observe exsolution homogeneously over the whole  $\text{La}_{0.2}\text{Sr}_{0.7}\text{Ti}_{0.9}\text{Ni}_{0.1}\text{O}_{3-\delta}$  thin film surface for all conditions. We observe a particle size increase with increasing time and temperature, varying from  $11 \pm 5$  nm size, when the perovskite thin film was reduced at 800 °C for 10 h, up to  $52 \pm 12$  nm when the exsolution was performed at 1000 °C for 10 h (Figure 4b). Interestingly, the device switching properties correlated with the particle size distributions. This can be seen with two example switching curves, as shown in Figure 4c. With increasing particle size, the hysteresis opens and the

ratio of the high and low resistive state increases (Figure 4d). All switching curves and their resistance ratio evolutions over 50 cycles are collected in Figure S6 (Supporting Information) and the retention characteristics in Figure S7 (Supporting Information). The largest ratio between the high and low resistance state, 180, was observed for the largest Ni particles. These particles had an average diameter of  $52 \pm 12$  nm after exsolution at 1000 °C for 10 h. Importantly, the cycle-to-cycle variability of the low resistance state also improved with increasing particle size (Figure 4e). The ON state resistance coefficient of variation (CV) decreases below 5% for the largest particles around 50 nm, whereas the lowest CV below 2% is measured for the reference device (Figures 2 and 3); however, its ratio between the two states was only around 50.

The strongest performance in terms of resistance ratio and switching stability is observed with the largest Ni particles at around 50 nm. This suggests that an infinitely large particle or a continuous Ni layer will equally benefit the switching response. To test this hypothesis, we fabricated a model device with a sputtered Ni layer of 20 nm between the bottom electrode and the  $\text{SrTiO}_3$  switching oxide. The current–voltage response (Figure S8, Supporting Information) exhibits neither the high stability in the ON state nor the high resistance ratio characteristic of the devices with the nanoparticles (Figure 4e).

Collectively, these results confirm that the exsolved nanoparticles at the interface aid the switching response.

Please note that the devices cycled in this work are very large ( $\approx 160$   $\mu\text{m}$  in diameter). We avoided on purpose the use of any lithography step to avoid any degradation of the nanoparticle and present the most reliable data as possible in terms of safe device fabrication. We expect a major impact of the smaller nanoparticles when devices are scaled down in electrode size and film thickness toward a realistic device integration, and should be further addressed.

### 2.3. Switching Mechanism and the Role of Exsolved Ni Nanoparticles

The counter-eightwise polarity current–voltage curve (Figure 3a) points to a classical filamentary-type switching with a rupture of the reduced filament (reset) during a positive bias on the top electrode and a subsequent formation of the filament (set) at a negative bias. A larger particle size aided the switching stability in reducing the coefficient of variation in the ON state (Figure 4e) and in increasing the resistance ratio (Figure 4d). In the following we hypothesize several ways the large Ni particles may be acting to stabilize the ON state and improve the switching ratio. First, reducing the thickness of the amorphous  $\text{SrTiO}_3$  above the nanoparticle likely makes the filament shorter, which can reduce compositional and shape variations along its length. Second, the larger particles may increase the diameter of the filament, therefore making the filament more robust and increasing the defect concentration. This result has been previously achieved by increasing the compliance current during the SET transition in  $\text{HfO}_x$ -based devices.<sup>[57]</sup> Third, the large particles also possess a reduced density, which lowers the number of possible filaments. It becomes harder to form subfilaments, which can grow and become the active filaments during

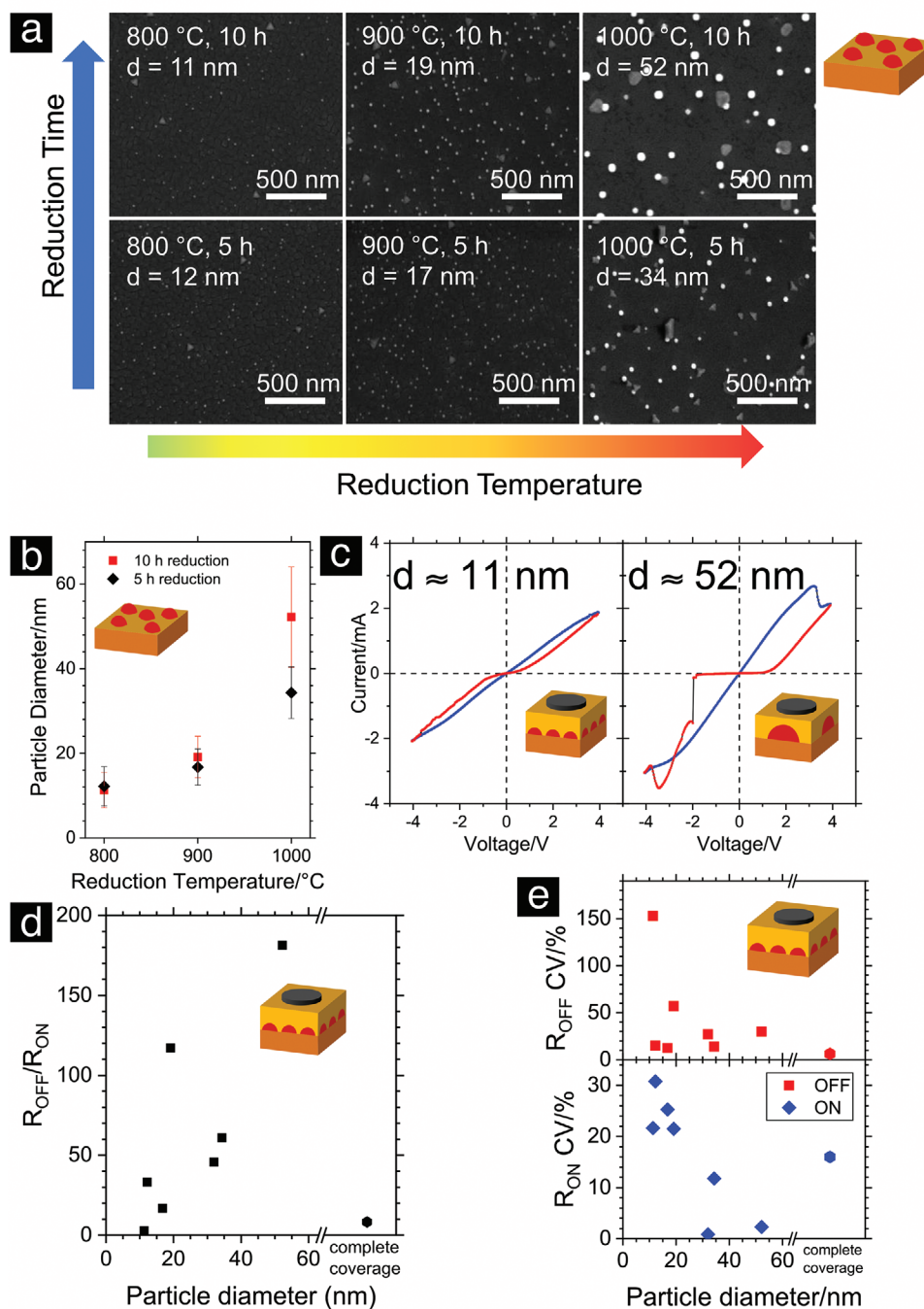


**Figure 4.** a) SEM micrographs of  $\text{La}_{0.2}\text{Sr}_{0.7}\text{Ti}_{0.9}\text{Ni}_{0.1}\text{O}_{3-\delta}$  thin films after reduction at different conditions. b) Average particle diameters resulting from SEM image analysis. c)  $I$ - $V$  profiles of devices with Ni particles with average diameters of 11.3 and 52.2 nm. d) Resistance ratios ( $R_{OFF}/R_{ON}$ ) measured over 50 consecutive switching cycles as a function of Ni particle diameters. e) Coefficients of variation of the resistances in the OFF and ON states versus particle diameters measured over 50 consecutive switching cycles. Panels (d) and (e) include the reference device (Figures 2 and 3) and the device with a continuous Ni bottom electrode (Figure S7, Supporting Information).

operation and lead to cycle-to-cycle variability. Fourth, the  $\text{SrTiO}_3$  film can be possibly distorted at its interface with the Ni particles. This distortion or its possible larger defect concentration can also contribute to a filament seeding effect. Lastly, both the stability of the ON state and the resistance ratio can be improved by an oxygen scavenging layer.<sup>[58]</sup> The oxygen scavenging poten-

tial of nickel is rather small when compared to other metals.<sup>[59]</sup> However the TEM analysis in Figure S1 (Supporting Information) reveals the formation of an oxide layer around the particles embedded in the  $\text{SrTiO}_3$  matrix, which may be further enlarged during the electroforming process. Larger Ni particles can offer a larger oxygen scavenging potential, similarly to previous

studies, where the thicker Ti scavenging layers reduce the SrTiO<sub>3</sub> switching films.<sup>[60]</sup> However, it has been suggested that rather than a high scavenging potential, a rational combination of the ohmic electrode layer and the switching oxide can stabilize the switching endurance.<sup>[45]</sup> The ohmic metal should have a lower stability than the parent (switching oxide) metal in order to facilitate fast oxygen exchange during the RESET process.<sup>[45]</sup> Ni has high formation energies (lies high in the Ellingham diagram) and can therefore provide fast oxygen release during the RESET operation. The ultimate reason for the observed improvement remains elusive and it is definitely worth of further exploration toward the implementation of this strategy in realistic device array architectures.

In terms of device manufacturing, it is important to understand that all of the stabilization mechanisms described above depend on the relative size of the exsolved Ni nanoparticles compared to the switching film. Therefore, there exists a clear opportunity to scale the whole device (including the particles) and enable high density storage memories with “hot spots” that can confine the filaments, formed by defects in the switching oxide. Despite the stochastic nature of the exsolution process, the distribution of the particles can be adjusted to meet the demands of high-density memories and ensure that each device will have a nanoparticle integrated in its structure. We emphasize here that we do not intend to show an optimize switching cell, but rather to point out an alternative strategy for reducing variability in amorphous memristive cells. While we are aware that certain combinations of oxide fabrication routes, substrates/bottom electrodes and device designs can also lead to strong decrease in device-to-device and cycle-to-cycle variations, we would also like to suggest that a synergy of different strategies could potentially benefit the ultimate goal of suppressing filament variations. The methodology proposed here brings added value by providing a platform with well-anchored nanoparticles, exemplified here for the case of Ni, but that could be extended to other metals as well. Therefore, the combination of potential materials systems and electrodes to explore is large enough. Guidance from simulations could further help to determine the best conditions for realistic fabrication conditions in terms of metal to be exsolved, thickness/nanoparticle size ratio and density.

### 3. Conclusion

Device yield and variability, both cycle-to-cycle and device-to-device, of memristive devices remains one of the biggest challenges for their industrial adaptation. Meeting this challenge requires controlling the switching filaments, specifically their location and composition. Recent efforts in the field have concentrated on filament confinement through various device fabrication strategies, such as embedding nanoparticles or confining the filament into a single dislocation. However, these fabrication methods are often not suitable for large scale production or require additional deposition steps.

In this work, we propose an alternative device fabrication route for embedding metal nanoparticles at the electrode-switching oxide interface in order to improve the cycle-to-cycle variability of a SrTiO<sub>3</sub>-based device. For this development, we

use exsolution processing, a method usually employed for catalysis in automotive exhaust control or solid oxide fuel/electrolysis cells, and expand the realm of applications of this technique into the field of memristive devices. By controlling the exsolution processing time and temperature of the bottom perovskite electrode, we can grow metal particles, here Ni, in situ with sizes between about 10 and 50 nm. These particles are naturally anchored in the bottom electrode backbone and offer high stability. We observe that increasing the nanoparticle diameter by a factor of 5 increases the ON/OFF resistance ratio from single units up to 180 and decreases the variability of the low resistance state below 5%. This improvement in the coefficient of variability (CV) in the low resistance state of about 90% compares well with previous reports on switching in HfO<sub>x</sub> ( $x < 2$ ) with embedded Pt nanocrystals<sup>[23]</sup> and exceeds the improvements in reports of Pt nanocrystals in TiO<sub>2</sub>.<sup>[32]</sup>

The improvement in the resistive switching characteristics is possible by the local enhancement of the electrical field, which confines the conductive filaments at the Ni nanoparticles, and the possibility of controlled oxygen exchange between the particle and the switching oxide during device operation.

We use amorphous SrTiO<sub>3</sub> as the switching oxide in this proof-of-concept device. Amorphous oxides are particularly attractive for resistive switches due to their low processing temperature (industrially viable) and, in some cases such as LaFeO<sub>3</sub>, increased oxygen ion diffusion coefficients.<sup>[61]</sup> By confining the switching filament on exsolved nanoparticles we can further improve their performance. As potential electrode materials, perovskite systems offer a high variety of possible cations to exsolve into metallic nanoparticles integrated into resistive switching devices. This makes exsolution-active perovskite electrodes very attractive for future memristive devices in terms of both filament confinement and device fabrication. Collectively, the results reported here introduce new strategies of improving cycle-to-cycle variability, often a big challenge with the random nanoionic processes governing memristive devices.

### 4. Experimental Section

**Device Fabrication:** The bottom electrode composition La<sub>0.2</sub>Sr<sub>0.7</sub>Ti<sub>0.9</sub>Ni<sub>0.1</sub>O<sub>3-δ</sub> was chosen with an A-site deficiency (when compared to the stoichiometric perovskite composition ABO<sub>3</sub>), in order to promote the exsolution process.<sup>[54]</sup> It was deposited with a thickness of ≈150 nm by pulsed laser deposition on a (100) oriented LaAlO<sub>3</sub> substrate (MTI Corp., USA) employing a KrF excimer laser (248 nm wavelength, Coherent, USA). The deposition was carried out at a temperature of 750 °C and an oxygen background pressure of 0.065 mbar for 4000 shots at a fluence of 1.9 J cm<sup>-2</sup> and a frequency of 2 Hz. Subsequent exsolution resulted in the condensation of Ni particles on the surface of the thin film. Exsolution was performed in a tube furnace using a 5% H<sub>2</sub>/Ar atmosphere (Airgas). The reduction temperature was varied between 800 and 1000 °C and the reduction time between 5 and 10 h. Amorphous SrTiO<sub>3</sub> (50 nm) was grown in a second pulsed laser deposition at a temperature of 150 °C and an oxygen background pressure of 0.027 mbar for 750 shots at a fluence of 1.9 J cm<sup>-2</sup> and a frequency of 2 Hz. Circular Pt top electrodes (80 nm thick) were grown by DC magnetron sputtering (Kurt J. Lesker, USA) at room temperature using a metal target of 99.99% pure Pt (ACI Alloys, USA), an Ar plasma at a pressure of 10 mTorr and a power of 50 W. The electrodes were defined by a metal shadow mask and had a diameter of 160 μm.

**Materials Characterization:** Scanning electron microscopy (Carl Zeiss Merlin HR-SEM, Germany) was employed to characterize the size and size distribution of exsolved Ni nanoparticles on thin films. Image analysis was performed using ImageJ 1.52a.<sup>[62]</sup>

Thin film X-ray diffraction (XRD) (Bruker D8 High-Resolution Diffractometer, Germany) was used to investigate  $\text{La}_{0.2}\text{Sr}_{0.7}\text{Ti}_{0.9}\text{Ni}_{0.1}\text{O}_{3-\delta}$  thin films before and after exsolution and the  $\text{SrTiO}_3$  switching oxide both grown on  $\text{LaAlO}_3$ .  $2\theta$ - $\omega$  spectra were recorded around the pseudocubic (200)  $\text{LaAlO}_3$  substrate peak.

High-resolution transmission electron microscopy (HR-TEM) and scanning transmission electron microscopy (STEM) were performed on an aberration-corrected FEI Titan S 80-300 STEM/TEM microscope equipped with a Gatan OneView camera at an acceleration voltage of 300 kV. Energy-dispersive X-ray spectroscopy (EDS) was performed with a large active area (60 mm<sup>2</sup>) EDAX silicon drift detector (SDD) at an acceleration voltage of 300 kV. All S/TEM specimens were prepared by FIB lift out using an FEI Nova 200 dual beam microscope. All specimens were thinned to electron transparency using a Fischione 1010 Ion Mill at a temperature below  $-100$  °C.

Atomic Force Microscopy measurements were performed on a Cypher, from Asylum Research.

**Device Characterization:** Cyclic voltammetry (Keithley 2601B System SourceMeter, USA) was employed to characterize the performance of the memristive model device. Measurements were performed in synthetic air (relative humidity <5%). Bias was applied to the top electrode while the bottom electrode was grounded. The devices were initialized by performing an electroforming step by holding a limiting current of 1 mA for 30 s. Cycling was carried out in the range of  $\pm 3$  or  $\pm 4$  V at a rate of 200 mV s<sup>-1</sup>. The obtained current-voltage curves were linearly fitted in the range of  $\pm 200$  mV in order to extract the resistance values of the OFF and ON states.

## Supporting Information

Supporting Information is available from the Wiley Online Library or from the author.

## Acknowledgements

J.S. and E.S. contributed equally to this work. This work was supported by the Swiss National Science Foundation Starting Grant (Grant NO. BSSGI0\_155986/1). This work made use of the MRSEC Shared Experimental Facilities at MIT, supported by the National Science Foundation under award number DMR-14-19807. A portion of this research was conducted at the Center for Nanophase Materials Sciences, which is a DOE Office of Science User Facility. This work was performed in part at the Center for Nanoscale Systems (CNS), a member of the National Nanotechnology Coordinated Infrastructure Network (NNCI), which was supported by the National Science Foundation under NSF award number 1541959. CNS is part of Harvard University.

## Conflict of Interest

The authors declare no conflict of interest.

## Keywords

exsolution, filament confinement, memristors, resistive switching, strontium titanate

Received: May 24, 2020

Revised: July 22, 2020

Published online: September 17, 2020

- [1] B. J. Choi, A. C. Torrezan, J. P. Strachan, P. G. Kotula, A. J. Lohn, M. J. Marinella, Z. Li, R. S. Williams, J. J. Yang, *Adv. Funct. Mater.* **2016**, *26*, 5290.
- [2] S. Pi, C. Li, H. Jiang, W. Xia, H. Xin, J. J. Yang, Q. Xia, *Nat. Nanotechnol.* **2019**, *14*, 35.
- [3] Q. Xia, J. J. Yang, *Nat. Mater.* **2019**, *18*, 309.
- [4] M. Aono, R. Waser, *Nat. Mater.* **2007**, *6*, 833.
- [5] Z. Wang, S. Joshi, S. Savel'ev, W. Song, R. Midya, Y. Li, M. Rao, P. Yan, S. Asapu, Y. Zhuo, H. Jiang, P. Lin, C. Li, J. H. Yoon, N. K. Upadhyay, J. Zhang, M. Hu, J. P. Strachan, M. Barnell, Q. Wu, H. Wu, R. S. Williams, Q. Xia, J. J. Yang, *Nat. Electron.* **2018**, *1*, 137.
- [6] J. C. Gonzalez-Rosillo, M. Balaish, Z. D. Hood, N. Nadkarni, D. Fraggedakis, K. J. Kim, K. M. Mullin, R. Pfenninger, M. Z. Bazant, J. L. M. Rupp, *Adv. Mater.* **2020**, *32*, 1907465.
- [7] Z. Wang, S. Joshi, S. E. Savel'ev, H. Jiang, R. Midya, P. Lin, M. Hu, N. Ge, J. P. Strachan, Z. Li, Q. Wu, M. Barnell, G.-L. Li, H. L. Xin, R. S. Williams, Q. Xia, J. J. Yang, *Nat. Mater.* **2017**, *16*, 101.
- [8] C. Baeumer, R. Valenta, C. Schmitz, A. Locatelli, T. O. Menteş, S. P. Rogers, A. Sala, N. Raab, S. Nemsak, M. Shim, C. M. Schneider, S. Menzel, R. Waser, R. Dittmann, *ACS Nano* **2017**, *11*, 6921.
- [9] K. Szot, W. Speier, G. Bihlmayer, R. Waser, *Nat. Mater.* **2006**, *5*, 312.
- [10] S. Choi, S. H. Tan, Z. Li, Y. Kim, C. Choi, P.-Y. Chen, H. Yeon, S. Yu, J. Kim, *Nat. Mater.* **2018**, *17*, 335.
- [11] G. Niu, P. Calka, M. Auf der Maur, F. Santoni, S. Guha, M. Fraschke, P. Hamoumou, B. Gautier, E. Perez, C. Walczyk, C. Wenger, A. Di Carlo, L. Alff, T. Schroeder, *Sci. Rep.* **2016**, *6*, 25757.
- [12] H. Ling, M. Yi, M. Nagai, L. Xie, L. Wang, B. Hu, W. Huang, *Adv. Mater.* **2017**, *29*, 1701333.
- [13] K.-Y. Shin, Y. Kim, F. V. Antolinez, J. S. Ha, S.-S. Lee, J. H. Park, *Adv. Electron. Mater.* **2016**, *2*, 1600233.
- [14] Y. Kim, H. Choi, H. S. Park, M. S. Kang, K.-Y. Shin, S.-S. Lee, J. H. Park, *ACS Appl. Mater. Interfaces* **2017**, *9*, 38643.
- [15] B. K. You, J. M. Kim, D. J. Joe, K. Yang, Y. Shin, Y. S. Jung, K. J. Lee, *ACS Nano* **2016**, *10*, 9478.
- [16] W. Li, X. Song, X. Zhao, X. Zhang, R. Chen, X. Zhang, C. Jiang, J. He, X. Xiao, *Nano Energy* **2020**, *67*, 104213.
- [17] W. Xiao, W. Song, Y. Ping Feng, D. Gao, Y. Zhu, J. Ding, *J. Mater. Chem. C* **2020**, *8*, 1577.
- [18] H. J. Kim, T. H. Park, K. J. Yoon, W. M. Seong, J. W. Jeon, Y. J. Kwon, Y. Kim, D. E. Kwon, G. S. Kim, T. J. Ha, S. G. Kim, J. H. Yoon, C. S. Hwang, *Adv. Funct. Mater.* **2019**, *29*, 1806278.
- [19] J. Lee, C. Du, K. Sun, E. Kioupakis, W. D. Lu, *ACS Nano* **2016**, *10*, 3571.
- [20] Y. Tao, X. Li, Z. Wang, H. Xu, W. Ding, J. Ma, Y. Liu, *Appl. Phys. Lett.* **2017**, *111*, 183504.
- [21] X. Zhao, J. Ma, X. Xiao, Q. Liu, L. Shao, D. Chen, S. Liu, J. Niu, X. Zhang, Y. Wang, R. Cao, W. Wang, Z. Di, H. Lv, S. Long, M. Liu, *Adv. Mater.* **2018**, *30*, 1705193.
- [22] X. Zhao, S. Liu, J. Niu, L. Liao, Q. Liu, X. Xiao, H. Lv, S. Long, W. Banerjee, W. Li, S. Si, M. Liu, *Small* **2017**, *13*, 1603948.
- [23] J. Wang, L. Li, H. Huyan, X. Pan, S. S. Nonnenmann, *Adv. Funct. Mater.* **2019**, *29*, 1808430.
- [24] W. Banerjee, S. Maikap, C.-S. Lai, Y.-Y. Chen, T.-C. Tien, H.-Y. Lee, W.-S. Chen, F. T. Chen, M.-J. Kao, M.-J. Tsai, J.-R. Yang, *Nanoscale Res. Lett.* **2012**, *7*, 194.
- [25] W.-Y. Chang, K.-J. Cheng, J.-M. Tsai, H.-J. Chen, F. Chen, M.-J. Tsai, T.-B. Wu, *Appl. Phys. Lett.* **2009**, *95*, 042104.
- [26] L. Gao, Y. Li, Q. Li, Z. Song, F. Ma, *Nanotechnology* **2017**, *28*, 215201.
- [27] A. Hao, M. Ismail, S. He, N. Qin, W. Huang, J. Wu, D. Bao, *RSC Adv.* **2017**, *7*, 46665.
- [28] Z. Xu, M. Gao, L. Yu, L. Lu, X. Xu, Y. Jiang, *ACS Appl. Mater. Interfaces* **2014**, *6*, 17823.
- [29] J. H. Yoon, J. H. Han, J. S. Jung, W. Jeon, G. H. Kim, S. J. Song, J. Y. Seok, K. J. Yoon, M. H. Lee, C. S. Hwang, *Adv. Mater.* **2013**, *25*, 1987.

- [30] J. H. Yoon, K. M. Kim, M. H. Lee, S. K. Kim, G. H. Kim, S. J. Song, J. Y. Seok, C. S. Hwang, *Appl. Phys. Lett.* **2010**, *97*, 232904.
- [31] W. Guan, S. Long, R. Jia, M. Liu, *Appl. Phys. Lett.* **2007**, *91*, 062111.
- [32] D. Sakellaropoulos, P. Bousoulas, D. Tsoukalas, *J. Appl. Phys.* **2019**, *126*, 044501.
- [33] W. Banerjee, Q. Liu, S. Long, H. Lv, M. Liu, *J. Phys. D: Appl. Phys.* **2017**, *50*, 303002.
- [34] Q. Liu, S. Long, H. Lv, W. Wang, J. Niu, Z. Huo, J. Chen, M. Liu, *ACS Nano* **2010**, *4*, 6162.
- [35] S.-C. Qin, R.-X. Dong, X.-L. Yan, *Appl. Phys. A* **2015**, *118*, 605.
- [36] N. Raab, D. O. Schmidt, H. Du, M. Kruth, U. Simon, R. Dittmann, *Nanomaterials* **2018**, *8*, 869.
- [37] L. Shi, D. S. Shang, Y. S. Chen, J. Wang, J. R. Sun, B. G. Shen, *J. Phys. D: Appl. Phys.* **2011**, *44*, 455305.
- [38] M. Uenuma, B. Zheng, K. Kawano, M. Horita, Y. Ishikawa, I. Yamashita, Y. Uraoka, *Appl. Phys. Lett.* **2012**, *100*, 083105.
- [39] Z. Q. Wang, H. Y. Xu, L. Zhang, X. H. Li, J. G. Ma, X. T. Zhang, Y. C. Liu, *Nanoscale* **2013**, *5*, 4490.
- [40] H. Mao, Z. Zhou, X. Wang, C. Ban, Y. Ding, T. Sun, Y. Yin, Z. Liu, J. Liu, W. Huang, *Adv. Electron. Mater.* **2019**, *5*, 1800503.
- [41] Y. Hayakawa, A. Himeno, R. Yasuhara, W. Boullart, E. Vecchio, T. Vandeweyer, T. Witters, D. Crotti, M. Jurczak, S. Fujii, S. Ito, Y. Kawashima, Y. Ikeda, A. Kawahara, K. Kawai, Z. Wei, S. Muraoka, K. Shimakawa, T. Mikawa, S. Yoneda, in *2015 Symp. on VLSI Technology (VLSI Technology)*, IEEE, Kyoto, Japan, June **2015**, pp. T14–T15, <https://doi.org/10.1109/VLSITechnology35523.2015>.
- [42] B. J. Choi, A. C. Torrezan, K. J. Norris, F. Miao, J. P. Strachan, M.-X. Zhang, D. A. A. Ohlberg, N. P. Kobayashi, J. J. Yang, R. S. Williams, *Nano Lett.* **2013**, *13*, 3213.
- [43] A. J. Carrillo, K. J. Kim, Z. D. Hood, A. H. Bork, J. L. M. Rupp, *ACS Appl. Energy Mater.* **2020**, *3*, 4569.
- [44] Y. Yang, P. Gao, L. Li, X. Pan, S. Tappertzhofen, S. Choi, R. Waser, I. Valov, W. D. Lu, *Nat. Commun.* **2014**, *5*, 4232.
- [45] W. Kim, S. Menzel, D. J. Wouters, Y. Guo, J. Robertson, B. Roesgen, R. Waser, V. Rana, *Nanoscale* **2016**, *8*, 17774.
- [46] B. Hua, M. Li, Y.-F. Sun, J.-H. Li, J.-L. Luo, *ChemSusChem* **2017**, *10*, 3333.
- [47] Y. Nishihata, J. Mizuki, T. Akao, H. Tanaka, M. Uenishi, M. Kimura, T. Okamoto, N. Hamada, *Nature* **2002**, *418*, 164.
- [48] X. Li, L. Dai, Z. He, W. Meng, Y. Li, L. Wang, *Sens. Actuators, B* **2019**, *298*, 126827.
- [49] S.-K. Otto, K. Kousi, D. Neagu, L. Bekris, J. Janek, I. S. Metcalfe, *ACS Appl. Energy Mater.* **2019**, *2*, 7288.
- [50] G. Tsekouras, D. Neagu, J. T. S. Irvine, *Energy Environ. Sci.* **2013**, *6*, 256.
- [51] D. Neagu, V. Kyriakou, I.-L. Roiban, M. Aouine, C. Tang, A. Caravaca, K. Kousi, I. Schreur-Piet, I. S. Metcalfe, P. Vernoux, M. C. M. van de Sanden, M. N. Tsampas, *ACS Nano* **2019**, *13*, 12996.
- [52] K. J. Kim, H. Han, T. Defferriere, D. Yoon, S. Na, S. J. Kim, A. M. Dayaghi, J. Son, T.-S. Oh, H. M. Jang, G. M. Choi, *J. Am. Chem. Soc.* **2019**, *141*, 7509.
- [53] H. Tanaka, M. Uenishi, M. Taniguchi, I. Tan, K. Narita, M. Kimura, K. Kaneko, Y. Nishihata, J. Mizuki, *Catal. Today* **2006**, *117*, 321.
- [54] D. Neagu, G. Tsekouras, D. N. Miller, H. Ménard, J. T. S. Irvine, *Nat. Chem.* **2013**, *5*, 916.
- [55] D. Cooper, C. Baeumer, N. Bernier, A. Marchewka, C. La Torre, R. E. Dunin-Borkowski, S. Menzel, R. Waser, R. Dittmann, *Adv. Mater.* **2017**, *29*, 1700212.
- [56] A. Marchewka, B. Roesgen, K. Skaja, H. Du, C.-L. Jia, J. Mayer, V. Rana, R. Waser, S. Menzel, *Adv. Electron. Mater.* **2016**, *2*, 1500233.
- [57] S. Balatti, S. Ambrogio, D. C. Gilmer, D. Ielmini, *IEEE Electron Device Lett.* **2013**, *34*, 861.
- [58] X. Zhong, I. Rungger, P. Zapol, H. Nakamura, Y. Asai, O. Heinonen, *Phys. Chem. Chem. Phys.* **2016**, *18*, 7502.
- [59] C. Chen, S. Gao, F. Zeng, G. S. Tang, S. Z. Li, C. Song, H. D. Fu, F. Pan, *J. Appl. Phys.* **2013**, *114*, 014502.
- [60] S. Stille, C.h. Lenser, R. Dittmann, A. Koehl, I. Krug, R. Muenstermann, J. Perlich, C. M. Schneider, U. Klemradt, R. Waser, *Appl. Phys. Lett.* **2012**, *100*, 223503.
- [61] R. Schmitt, M. Kubicek, E. Sediva, M. Trassin, M. C. Weber, A. Rossi, H. Hutter, J. Kreisel, M. Fiebig, J. L. M. Rupp, *Adv. Funct. Mater.* **2019**, *29*, 1804782.
- [62] C. A. Schneider, W. S. Rasband, K. W. Eliceiri, *Nat. Methods* **2012**, *9*, 671.